



Theoretical modeling, experimental validation, and thermodynamic analysis on intermediate heat-exchange cycle system

Weitong Liu^{a,b,c}, Guoqiang Xu^{a,b,c}, Xiaojia Gang^{a,b,c}, Han Qi^{b,c}, Mowen Li^d, Jie Wen^{a,b,c}, Yanchen Fu^{a,b,c,*}

^a Research Institute of Aero-engine, Beihang University, Beijing 100191, China

^b Collaborative Innovation Center for Advanced Aero-Engine, Beihang University, Beijing 100191, China

^c Frontiers Science Center for Super-cycle Aeroengine's Aerothermodynamics, Beihang University, Beijing 100191, China

^d Beijing Power Machinery Institute, Beijing 100074, China



ARTICLE INFO

Keywords:

Heat transfer system
Experimental analysis
Energy flow model
Aero engine

ABSTRACT

The focus of this study is to explore the thermodynamic characteristics of an intermediate heat-exchange cycle (IHEC) system in aero engines, employing experimental analysis. Using air, fuel, and intermediate working fluid (IWF) as working mediums, an IHEC system experimental platform incorporated two heat exchangers (HEX) was established. A theoretical analysis model for characteristics of the IHEC system was developed using the heat current method and a novel method for estimating the overall heat transfer coefficient (K). Deviations between experimental and simulation results for system equilibrium heat transfer rates and temperatures at each node of the IHEC system are within $\pm 10\%$, and the maximum average relative deviation of the proposed method for estimating K is -7.93% . Detailed analyses have been conducted regarding the effects of fuel mass flow rate, IWF mass flow rate, air mass flow rate, and air inlet temperature on the system. Raising the fuel mass flow rate leads to reduced temperatures at each system node, while the system's equilibrium heat transfer rate initially increases and then stabilizes. Variations in IWF mass flow rate have complex impacts on the IHEC system, influenced by HEX design margins and heat transfer capacities. Tailored analyses are necessary based on specific circumstances.

1. Introduction

Ensuring sufficient and effective thermal management poses a growing challenge for both civil and military aircraft. The primary attribution for this lies in the noteworthy increase in the magnitude of heat loads onboard, as well as their variable characteristics, including the existence of low-grade heat sources, and the inability to expel certain waste heat through engine exhaust gases. Formerly, the issue of thermal management was associated with aircraft experiencing excessive aerodynamic heating at high Mach numbers. However, as internal heat loads increase in both magnitude and quantity, design considerations for subsonic aircraft are being progressively influenced [1]. Currently, researchers generally put the spotlight on thermal management technologies for aero engines in two ways: cycle process design and cycle parameters tweaking [2].

Cycle process is designed to meet the thermal requirements in the propulsion. Comprehensive investigations have been conducted to

assess promising engine configurations, such as the Precooled Turbine Combined Cycle (PTCC) [3], the Rocket-based Combined Cycle (RBCC) [4], and the Turbine-based Combined Cycle (TBCC) [5]. Nevertheless, during hypersonic flight, both the conventional TBCC and RBCC encounter significant technical challenges related to mode conversion and thermal protection [6]. Compared with them, the PTCC engine incorporates well-established technologies, such as the turbomachinery and HEX [7]. To this end, PTCC is being developed and put into use, representatives including LACE [8], ACES [9], ATRDC [10], ATREX [11], KLIN [12], SABRE [13], PATR [14], MIPCC [15], and so forth. Recently, Zou et al. [16] introduced a helium closed-cycle layout for the Hypersonic Air-breathing Precooled Engine, aiming for an improved balance between system complexity and the specific impulse. The proposed helium closed cycle utilizes a recompression and two-branches cooling scheme. Wang et al. [17] suggested a multi-stage precooling compression cycle, incorporating the reuse of the fuel through the transfer of heat energy to mechanical work.

Cooled Cooling Air (CCA) technology is a typical representative of

* Corresponding author at: Research Institute of Aero-engine, Beihang University, Beijing 100191, China.

E-mail address: yanchenfu@buaa.edu.cn (Y. Fu).

Nomenclature	
A	heat transfer area of HEX [m ²]
a	coefficient
b	coefficient
C	coefficient
c_p	isobaric specific heat capacity [J/kg/K]
d	hydraulic diameter [mm]
h	heat transfer coefficient [W/m ² /K]
K	overall heat transfer coefficient [W/m ² /K]
m	mass flow rate [kg/s]
Nu	Nusselt number
Pr	Prandtl number
P	pressure [MPa]
Q	heat transfer rate [W]
Q_{equal}	equilibrium heat transfer rate [W]
R	inlet temperature difference-based thermal resistance [K/W]
R_{wall}	thermal resistance of the wall [K/W]
Re	Reynolds number
T	temperature [°C]
T_1	IWF inlet temperature of HEX-1 [°C]
T_2	IWF outlet temperature of HEX-1 [°C]
ΔT_m	logarithmic mean temperature difference [°C]
Greek symbols	
α	calculation coefficient, $\alpha = \left(\frac{4}{\mu_c \pi} \right)^a \frac{C_{h_c} P r_c^b}{d_c^{a+1}}$
β	calculation coefficient, $\beta = A R_{wall} + \frac{A}{h_h A_h}$
μ	dynamic viscosity [μPa·s]
λ	thermal conductivity [W/m/K]
Subscripts	
1	HEX-1
2	HEX-2
a	air
f	fuel
c	cold fluid
h	hot fluid
i	inlet
o	outlet
$w1$	intermediate working fluid in HEX-1
$w2$	intermediate working fluid in HEX-2
w	intermediate working fluid
Abbreviations	
ANN	Artificial neural networks approach
CCA	Cooled Cooling Air
HEX	Heat exchanger
HTC	Heat transfer coefficient
IHEC	Intermediate heat-exchange cycle
IWF	Intermediate working fluid
LMTD	Logarithmic mean temperature difference
PTCC	Precooled Turbine Combined Cycle
RBCC	Rocket-based Combined Cycle
TBCC	Turbine-based Combined Cycle

cycle parameters tweaking in the thermal management system. CCA technology effectively cools the compressor bleed air, fulfilling the growing thermal protection demands, by utilizing bypass stream air, inlet ram air, or fuel [18]. The growing intensity of heat sources on military aircraft has necessitated an amplified dependence on fuel serving the purpose of a coolant. The attractiveness of using fuel as a heat sink on aero engines results from multiple reasons, including better cooling effectiveness than air, proximity to systems requiring cooling, availability, and low temperature [1,19,20]. Duncan et al. [21] experimentally investigated the aerodynamic impact CCA technology has on the combustion system's external aerodynamics. Zhuang et al. [22] analyzed the impact of CCA technology on the aerothermal characteristics of a low bypass ratio aero-engine, highlighting distinct effects at various flight altitudes and Mach numbers. As to the CCA HEX, its aerothermal performance with flow nonuniformities was explored by Pandey et al. [23]. It is demonstrated heat transfer rate is notably reduced with the presence of cross-flow upstream of the HEX core.

Despite being regarded as promising approaches listed above for aero engines to provide adequate thermal management, there are still numerous challenges that need to be tackled. In PTCC engines, the third fluid is used for heat transfer, creating an IHEC, which introduces two or more HEXs [24]. Current research in the field of thermal transport primarily focuses on working fluids or thermal transport components, such as HEXs, pumps, control equipment, and so on. Nevertheless, the experimental investigation on the thermodynamic characteristics of the IHEC system is limited. In the research of Kasim et al. [25], the possible compact HEXs with novel heat transfer surface geometries were described. In the work by Chang et al. [26], a novel annular air-hydrogen precooler was introduced, demonstrating higher volumetric power and compactness, while the power per mass unit was lower than shell-tube HEX and plate-fin HEX. The liquid working fluids for aircraft thermal protection were introduced by Affonso et al. [27]. These include thermal oils, dielectric fluids, and ethylene glycol-water mixtures. Liu

et al. [28] experimentally explored the impact of working conditions on the intermediate circulation, and water was chosen as the only working fluid in their experiments. As for CCA technology, if an excessive amount of heat is transferred to the fuel, the temperature will reach its maximum allowable level. When this occurs, the aero engine has reached a point referred to as its thermal endurance limit [29–31]. According to Herring and Heister [32], thermo-acoustic oscillations and fuel coking posed considerable obstacles in the operation of the fuel-cooled HEXs. Moreover, issues in the manufacturing of the fuel-air HEX may lead to the exposure of fuel to the high-temperature air, potentially triggering a fire. However, the introduction of an IHEC system in aero engines facilitates the use of CCA technology without inherent safety risks by employing an IWF to avoid direct contact between air and fuel. Therefore, with regard to the thermal management of aero engines, whether it is PTCC or CCA technology, the current research gap primarily lies in the thermodynamic characteristics of the IHEC system in aero engines.

To directly understand and analyze the thermodynamic characteristics of the IHEC system, a highly efficient model method is strongly required. Current modeling methodologies rely on the physical analysis of individual components. These approaches stack the governing equations based on the component arrangement, leading to the formulation of a comprehensive mathematical model for the system. By solving these equations, it is possible to simulate the system, thereby enabling parametric analysis and optimization [33]. However, when it comes to a complex system, the above methods involve considerable governing equations requiring iterations owing to their inherent nonlinearity and it will consume a lot of computation time [34,35]. What's more, numerous initial values are required for the solving process, and the stability and efficiency of calculations are greatly influenced by their selection [36]. Building upon the entransy theory [37], Chen et al. [38,39] put forward the heat current method for conveniently analyzing and optimizing thermal systems based on the radiation-network approach and the thermo-electrical analogy method. The application of the heat current

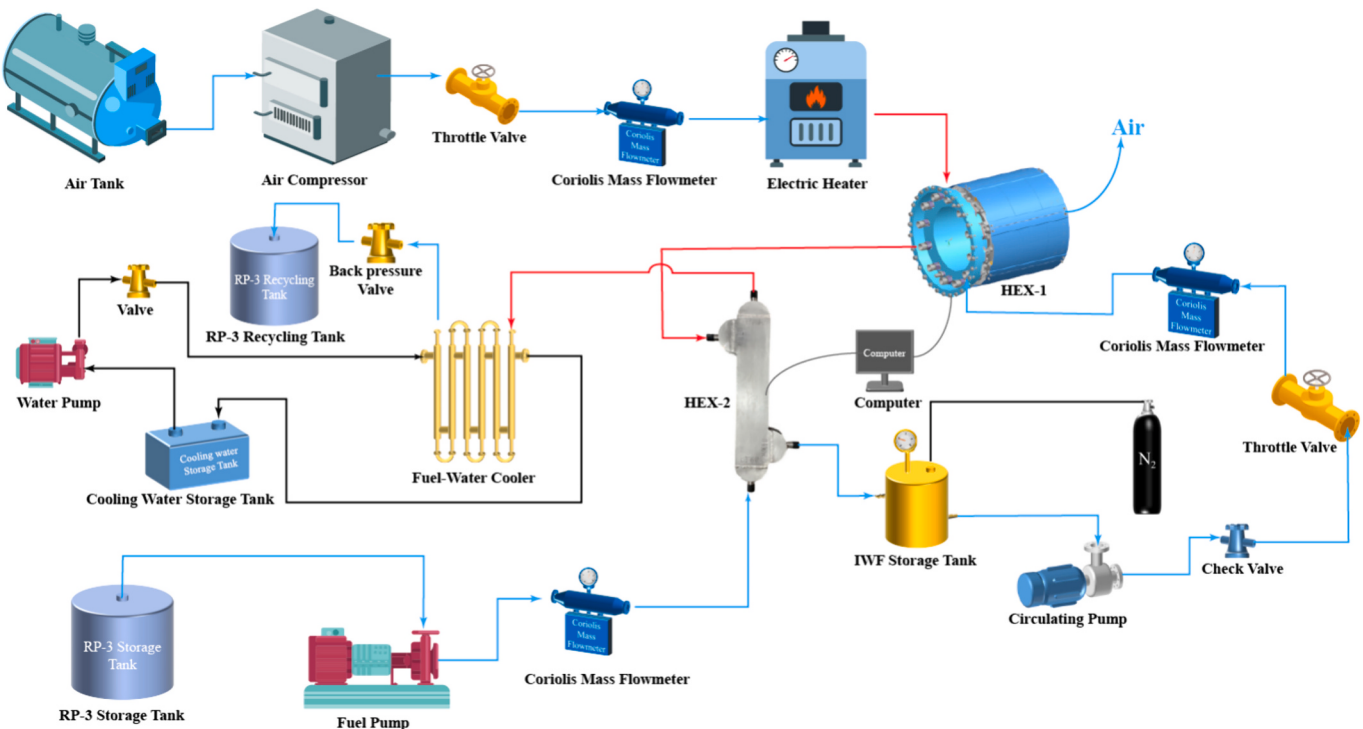


Fig. 1. Schematic diagram of the test rig for the IHEC system.

method has proven successful in a wide range of thermal systems, including aircraft environment control systems [40], Organic Rankine Cycle Systems [41], district heating systems [42], absorption energy storage systems [43], and so forth.

Despite the numerous advantages of the heat current method, there are still some pertinent considerations to be taken into account when utilizing it, particularly in relation to estimating the K of HEXs under different flight conditions. The artificial neural networks approach (ANN) is extensively employed for predicting the K . Goudarzi et al. [44] estimated the thermal contact conductance and suggested the Levenberg Marquardt algorithm. Zhang and A. Rahman [45] utilized ANN for predicting the oscillatory heat transfer coefficient (HTC) and proved the accuracy of the ANN model by comparing ANN model results with both published literature results and experimental results. Mini/micro-channels saturated flow boiling HTC has been predicted by Qiu et al. [46] using the ANN. However, the estimation of the K by using ANN still has some limits. The literature [46] pointed out that despite the improvement, certain results still exhibit a relatively high error rate of 39.6%, indicating that excluding the obtained HTC from the model was not feasible. Furthermore, it should be noted that ANN does not exhibit explicit and clear correlations that can be directly extrapolated to specialized cases. Although ANN offers the capability to fit curves and provide statistical predictions for HTC, it falls short in incorporating the physical laws [47]. In this context, it is necessary to build a K estimating model combined with the physical laws to utilize the heat current method conveniently and appropriately.

The present study experimentally investigates the thermodynamic characteristics of an IHEC system for aero engines. An experimental platform of a two-stage HEX combined IHEC system has been built using fuel, IWF, and air as working mediums. A theoretical analysis model of the system-level characteristics of the IHEC system is developed on the basis of the heat current method and the proposed method for estimating the K . The model's accuracy is subsequently validated through experimental data, and an exploration of the heat transportation principle of the system is conducted under varying operating conditions.

2. Experimental system and data reduction

2.1. Experimental system

The thermodynamic performance test rig for the IHEC system is depicted in Fig. 1. Four key sub-systems constitute the experimental setup: the IWF-path system, fuel-path system, air-path system, and cooling water-path system. For simulation purposes, high-temperature air serves as the heat source to imitate compressor bleed air, hydrocarbon fuel RP-3 at supercritical pressures is employed as the coolant, and the selected IWF for the system is high-pressure water to avoid boiling to maintain the stability of the system. Along the air path, adjusting and measuring the air mass flow rate is achieved using an electric control valve and a Coriolis mass flowmeter. Following this, an electric heater is employed to raise the air to a predetermined temperature. Subsequently, the high-temperature air exchanges heat with IWF in a serpentine tube HEX (HEX-1) and is directly discharged into the surroundings. Within the fuel pathway, RP-3 is pressurized by a triple plunger pump, sourced from the RP-3 storage tank at room temperature. Following its passage through a mass flowmeter, the fuel undergoes heating via the high-temperature IWF within an airfoil-fin printed circuit HEX (HEX-2). Afterward, the heated fuel undergoes cooling in a double-pipe water cooler and the fuel-path system pressure is regulated with a back-pressure valve. Ultimately, the fuel is recycled to the RP-3 tank as there is no coke production throughout the entire process. In the IWF path, before the experiment, use high-pressure nitrogen to pressurize the water in the IWF storage tank to the specific pressure. After that, high-pressure water is driven by a circulating pump and flows through a check valve used to prevent backflow. Adjusting the desired IWF mass flow rate is achieved with an electric control valve, while measurement is carried out using a mass flowmeter. Subsequently, IWF is heated by the air in HEX-1 after that flows into HEX-2 to be cooled by the fuel. Finally, IWF completes a closed cycle by returning to the IWF storage tank. As for the cooling water-path system, the double-pipe water cooler is adopted to cool the fuel.

To measure the pressure drop and absolute pressure in the fuel, air,

Table 1

Range and uncertainty of direct measurements.

Direct measurement	Range	Uncertainty
Air mass flow rate	0–0.5 kg/s	±0.5%
Fuel mass flow rate	0–0.5 kg/s	±0.2%
IWF mass flow rate	0–0.5 kg/s	±0.15%
Temperature	223.15–1423.15 K	±1.5 K
Absolute pressure	0–10 MPa	±0.04%
Absolute pressure	0–1 MPa	±0.04%
Pressure drop	0–300 kPa	±0.04%
Pressure drop	0–30 kPa	±0.04%
Pressure drop	0–20 kPa	±0.04%

and IWF paths, Rosemount's differential pressure transducers (Model 3051CD2) and absolute pressure transducers (Model 3051CA2, 3051CA4) are utilized. Temperatures at the inlet and outlet sides of HEX-1 and HEX-2 are obtained using K-type sheathed thermocouples. Multiple data acquisition modules ADAM 4118 collect all measured data, and these signals are then channeled to ADAM 4520 before being linked to an Industrial Personal Computer. Thermal insulation material is applied to all high-temperature pipelines and HEXs to reduce heat loss. **Table 1** provides the working range and uncertainty of direct measurements. **Fig. 2** shows the photograph of the experimental setup and its main components.

2.2. Data reduction

The determination of heat transfer rates to the air, fuel, and IWF involves analyzing the measured mass flow rates (m_a , m_f , m_w) and the temperatures of different working fluids, as below. The thermal properties of air and water and their uncertainties are obtained from the NIST [48]. The isobaric specific heat capacity and density of RP-3 are gained from the experimental results in the literature [49,50].

$$Q_a = m_a c_{p,a} (T_{a,i} - T_{a,o}) \quad (1)$$

$$Q_f = m_f c_{p,f} (T_{f,o} - T_{f,i}) \quad (2)$$

$$Q_{w1} = m_w c_{p,w1} (T_{w1,o} - T_{w1,i}) \quad (3)$$

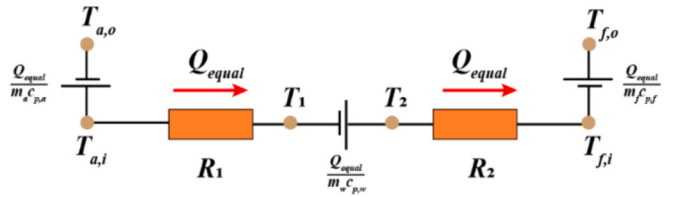
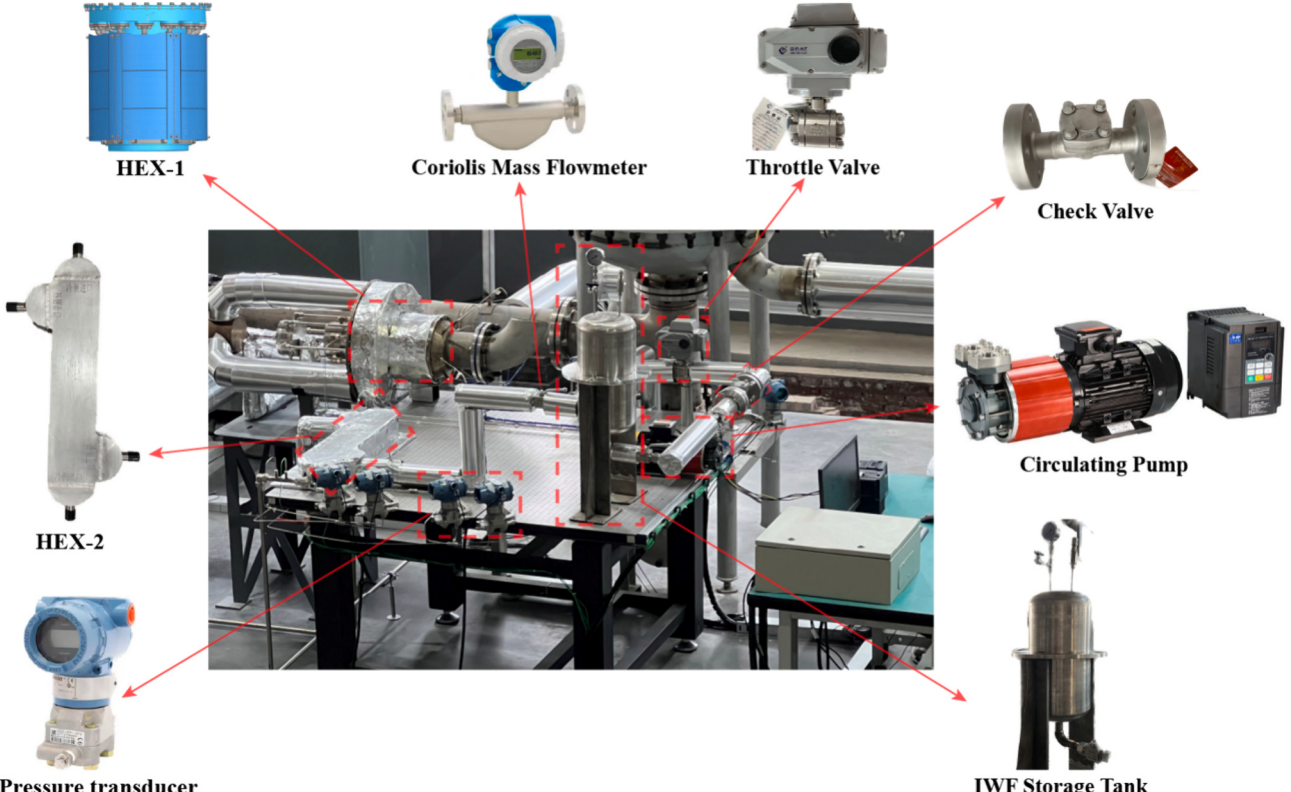
$$Q_{w2} = m_w c_{p,w2} (T_{w2,i} - T_{w2,o}) \quad (4)$$

where Q_a , Q_f , Q_{w1} , Q_{w2} is the Q of air, fuel, IWF within HEX-1, and IWF within HEX-2, respectively; $c_{p,a}$, $c_{p,f}$, $c_{p,w1}$, $c_{p,w2}$ is the c_p of air, fuel, IWF within HEX-1, and IWF within HEX-2, respectively; T_a , T_f , T_{w1} , T_{w2} is the temperature of air, fuel, IWF in HEX-1, and IWF in HEX-2, respectively, and subscript 'i' for inlet, 'o' for outlet.

Table 2

Uncertainties of the heat transfer rate and overall heat transfer coefficient.

Parameters	Uncertainty
Heat transfer rate of air (Q_a)	1.54%
Heat transfer rate of fuel (Q_f)	5.13%
Heat transfer rate of IWF (Q_{w1} or Q_{w2})	2.83%
Overall heat transfer coefficient of HEX-1 (K_1)	1.68%
Overall heat transfer coefficient of HEX-2 (K_2)	5.20%

**Fig. 3.** The energy flow model of the IHEC system.**Fig. 2.** A photograph of the experimental setup and its main components.

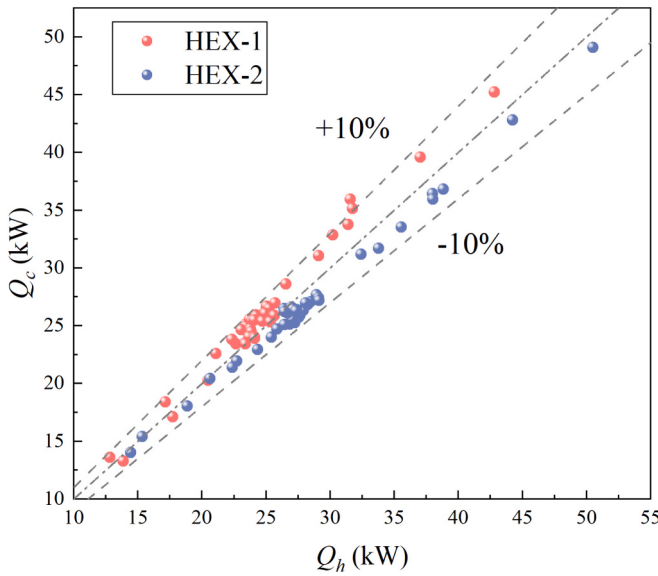


Fig. 4. Comparison of heat transfer rate between hot-side fluid and cold-side fluid for each HEX for all experimental data.

Table 3
Experimental parameters for variable air inlet temperature.

Parameter	Value	Parameter	Value
m_a (kg/s)	0.202	$T_{f,i}$ (°C)	34.0–44.0
m_w (kg/s)	0.102	$P_{a,i}$ (MPa)	0.103
m_f (kg/s)	0.233	$P_{w1,i}$ (MPa)	2.026
$T_{a,i}$ (°C)	152.0–399.5	$P_{f,i}$ (MPa)	2.995

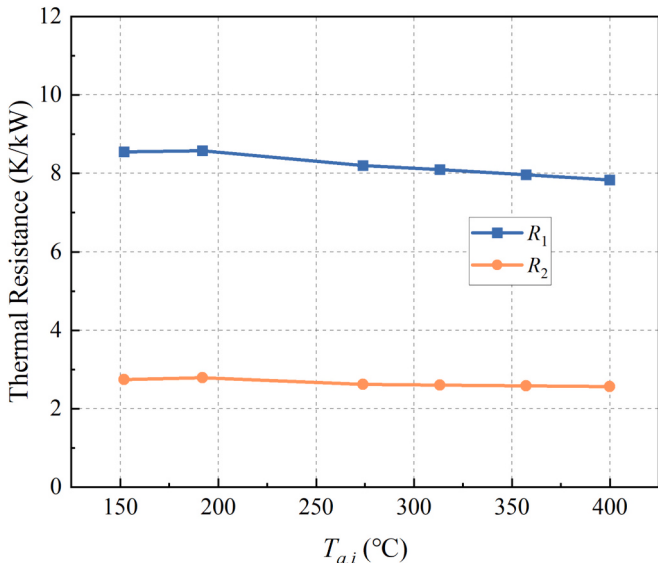


Fig. 5. Inlet temperature difference-based thermal resistance variations with air inlet temperature.

The average Q between hot side and cold side of HEX-1 and HEX-2 is calculated as follows:

$$Q_1 = (Q_a + Q_{w1})/2 \quad (5)$$

$$Q_2 = (Q_f + Q_{w2})/2 \quad (6)$$

For the IHEC system under investigation in this study, disregarding

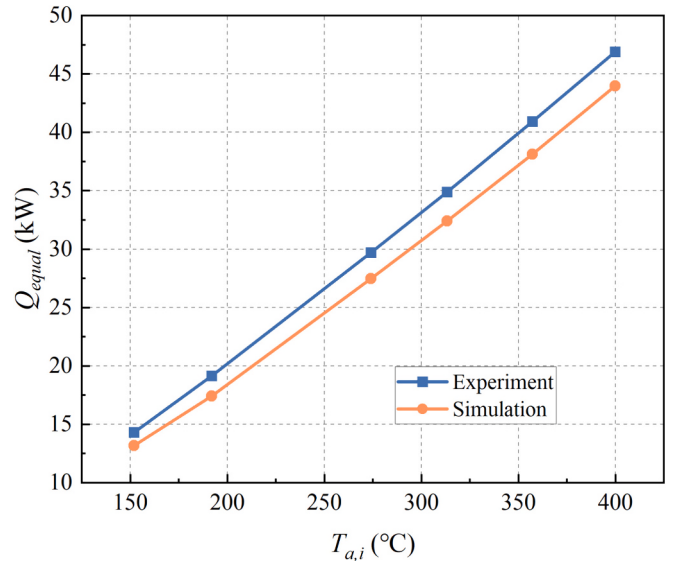


Fig. 6. Equilibrium heat transfer rate within the system variations with air inlet temperature.

heat losses, it can be inferred that Q_1 and Q_2 should be in equilibrium when the system reaches a stable state. Consequently, the system's equilibrium heat transfer rate is defined as Eq. (7). Moreover, for each HEX in the series layout, the IWF temperature should satisfy the following equations:

$$Q_{equal} = (Q_1 + Q_2)/2 = (Q_a + Q_f + Q_{w1} + Q_{w2})/4 \quad (7)$$

$$T_1 = T_{w1,i} = T_{w2,o} \quad (8)$$

$$T_2 = T_{w1,o} = T_{w2,i} \quad (9)$$

where T_1 is the IWF inlet temperature of HEX-1, T_2 is the IWF outlet temperature of HEX-1. Due to the neglect of heat losses, T_1 and T_2 correspond to the outlet and inlet temperatures of HEX-2, respectively.

HEXs within the system are all configured in a counterflow arrangement. The logarithmic mean temperature difference (LMTD) is computed by the following equations.

$$\Delta T_{m1} = \frac{(T_{a,i} - T_{w1,o}) - (T_{a,o} - T_{w1,i})}{\ln\left(\frac{T_{a,i} - T_{w1,o}}{T_{a,o} - T_{w1,i}}\right)} \quad (10)$$

$$\Delta T_{m2} = \frac{(T_{w2,i} - T_{f,o}) - (T_{w2,o} - T_{f,i})}{\ln\left(\frac{T_{w2,i} - T_{f,o}}{T_{w2,o} - T_{f,i}}\right)} \quad (11)$$

The K of each HEX can be obtained as:

$$K_1 = \frac{Q_1}{A_1 \Delta T_{m1}} \quad (12)$$

$$K_2 = \frac{Q_2}{A_2 \Delta T_{m2}} \quad (13)$$

where A is the heat exchange surface area of different HEXs.

2.3. Uncertainty analysis

The present study adopts the uncertainty analysis method described in Ref [51–53]. Assuming measurements with uncertainties $\delta x_1, \delta x_2, \dots, \delta x_n$ for variables x_1, x_2, \dots, x_n , the values obtained are utilized in the computation of the variable (y) as shown in Eq. (14). In the case of independent and random uncertainties in x_1, x_2, \dots, x_n , the uncertainty in

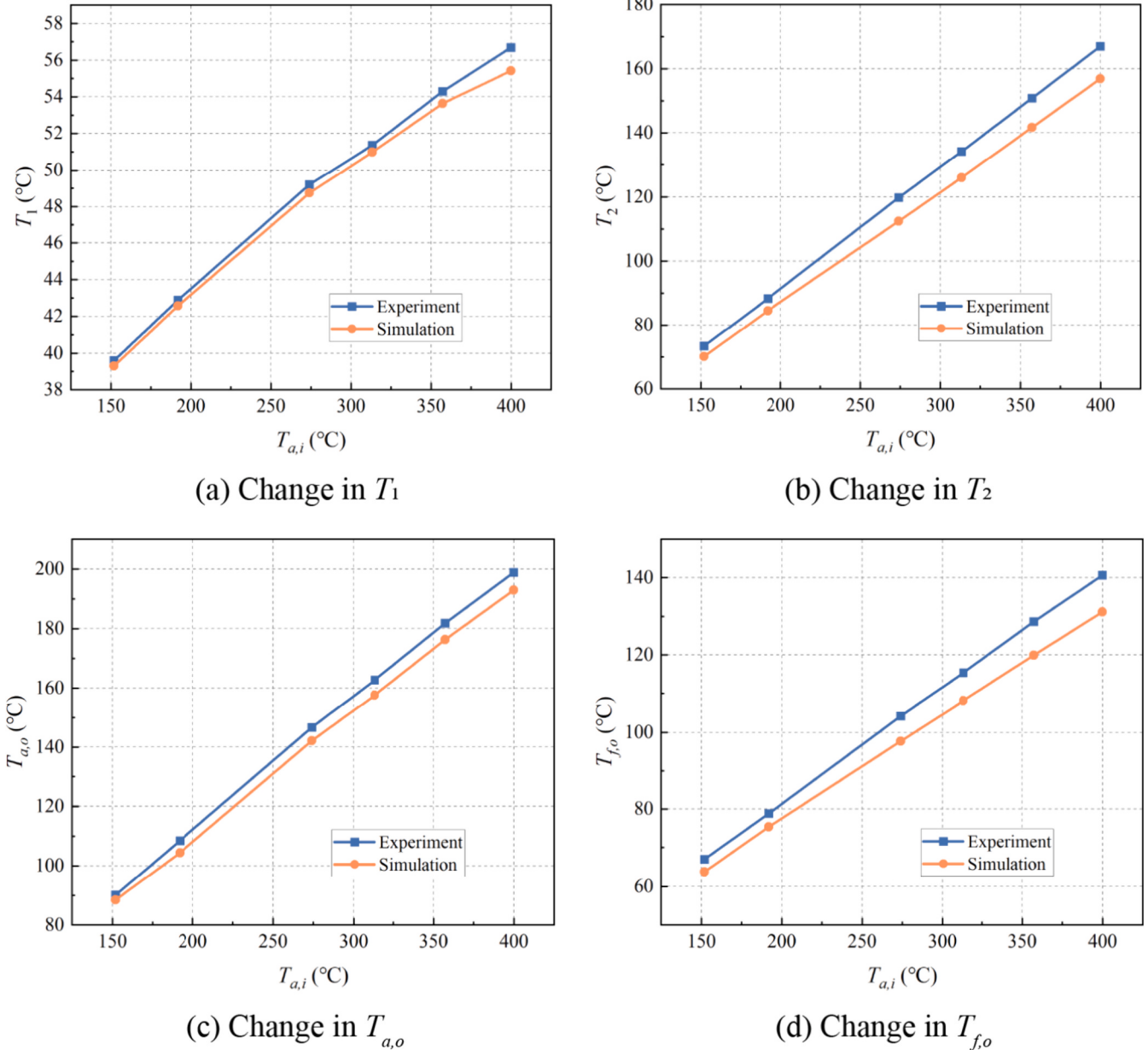


Fig. 7. Temperature variation with air inlet temperature at each node of the IHEC system.

y is:

$$y = f(x_1, x_2, \dots, x_n) \quad (14)$$

$$\delta y = \sqrt{\left(\frac{\partial y}{\partial x_1} \delta x_1\right)^2 + \left(\frac{\partial y}{\partial x_2} \delta x_2\right)^2 + \dots + \left(\frac{\partial y}{\partial x_n} \delta x_n\right)^2} \quad (15)$$

Combining the uncertainty of direct measurements, the uncertainties of Q and K of each HEX are detailed in Table 2.

3. Thermodynamic performance model for the IHEC system

Basically, incorporating actual operational conditions, there are four parameters that contribute to the thermodynamic characteristics of the IHEC system: $T_{a,i}$, m_a , m_f , and m_w . This study investigates the influence patterns of these four parameters and develops mathematical models on the basis of the heat current method and K estimating model, incorporating experimental data. By employing the theoretical analysis model, the temperature at each node of the IHEC system and the system's heat

load can be conveniently and quickly calculated when the high-temperature heat source inlet temperature $T_{a,i}$, low-temperature cold source inlet temperature $T_{f,i}$, and the mass flow rates of the three working mediums are known in the IHEC system.

3.1. Heat current model of IHEC

Employing the heat current method [36], it is possible to construct the energy flow model of the IHEC system by connecting state points with the same temperature, as presented in Fig. 3. The system's topological relations can be expressed through mathematical equations derived from Kirchhoff's voltage law as below:

$$T_{a,i} - T_{f,i} = Q_{equal}R_1 - \frac{Q_{equal}}{m_w c_{p,w}} + Q_{equal}R_2 \quad (16)$$

$$T_{a,i} - T_1 = Q_{equal}R_1 \quad (17)$$

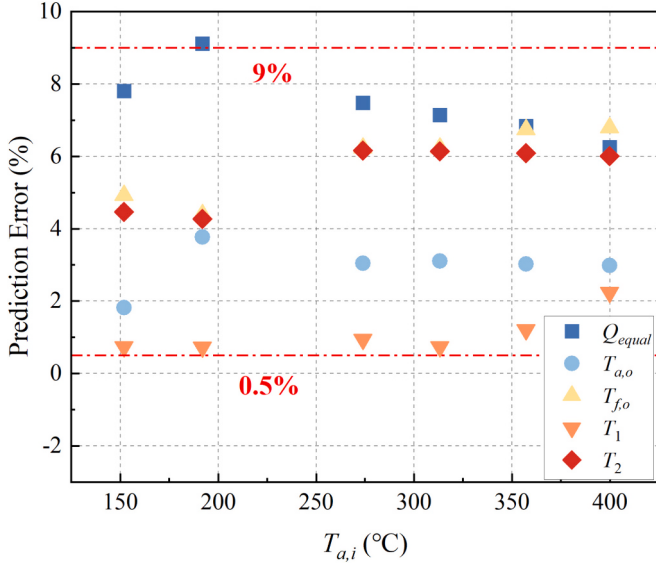


Fig. 8. Prediction errors of all parameters with different air inlet temperatures.

Table 4
Experimental parameters for variable air mass flow rate.

Parameter	Value	Parameter	Value
m_a (kg/s)	0.088–0.321	$T_{f,i}$ (°C)	25.0–35.6
m_w (kg/s)	0.104	$P_{a,i}$ (MPa)	0.103
m_f (kg/s)	0.234	$P_{w1,i}$ (MPa)	1.753
$T_{a,i}$ (°C)	243.9	$P_{f,i}$ (MPa)	2.965

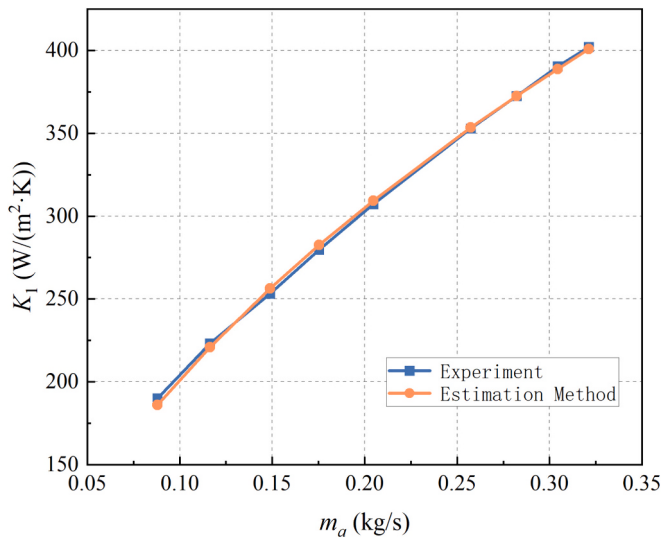


Fig. 9. Comparison of K_1 as a function of m_a between experimental and estimated results.

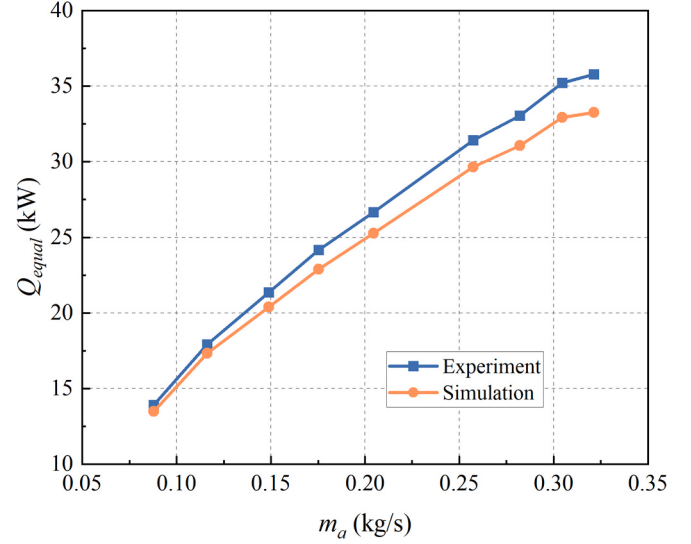


Fig. 10. Equilibrium heat transfer rate within the system variations with air mass flow rate.

$$T_{a,i} - T_2 = Q_{equal} R_1 - \frac{Q_{equal}}{m_w c_{p,w}} \quad (18)$$

$$T_{a,i} - T_{a,o} = \frac{Q_{equal}}{m_a c_{p,a}} \quad (19)$$

$$T_{f,o} - T_{f,i} = \frac{Q_{equal}}{m_f c_{p,f}} \quad (20)$$

The inlet temperature difference-based thermal resistance of HEX-1 and HEX-2 is defined as:

$$R_1 = \frac{m_w c_{p,w} \exp\left(\frac{K_1 A_1}{m_a c_{p,a}}\right) - m_a c_{p,a} \exp\left(\frac{K_1 A_1}{m_w c_{p,w}}\right)}{(m_a c_{p,a}) (m_w c_{p,w}) \left[\exp\left(\frac{K_1 A_1}{m_a c_{p,a}}\right) - \exp\left(\frac{K_1 A_1}{m_w c_{p,w}}\right) \right]} \quad (21)$$

$$R_2 = \frac{m_f c_{p,f} \exp\left(\frac{K_2 A_2}{m_w c_{p,w}}\right) - m_w c_{p,w} \exp\left(\frac{K_2 A_2}{m_f c_{p,f}}\right)}{(m_w c_{p,w}) (m_f c_{p,f}) \left[\exp\left(\frac{K_2 A_2}{m_w c_{p,w}}\right) - \exp\left(\frac{K_2 A_2}{m_f c_{p,f}}\right) \right]} \quad (22)$$

3.2. The approach to estimating the K of HEX

As depicted in Eqs. (21) and (22), a convenient and accurate estimation of K is the key to solving the model. This study presents a model for K estimation based on fluid mass flow rate through theoretical derivation. It pertains to the situation wherein the K of a HEX varies with the hot/cold-side fluid mass flow rate while maintaining a constant mass flow rate of the other side. The approach relies on the fundamental principles of heat transfer rather than statistical laws and involves the incorporation of adjustable coefficient constants based on experimental data to establish an adequate correlation. To simplify the model, the K estimation model of HEX is built upon the following assumptions: 1) the thermal properties of working mediums are constant; 2) the HTC remains consistent in the fluid with a constant mass flow rate, while the HTC of the other fluid varies with the flow conditions.

The K of HEX can be written as:

$$K = \frac{1}{A \left(\frac{1}{h_e A_e} + R_{wall} + \frac{1}{h_h A_h} \right)} \quad (23)$$

where R_{wall} represents the thermal resistance attributed to thermal

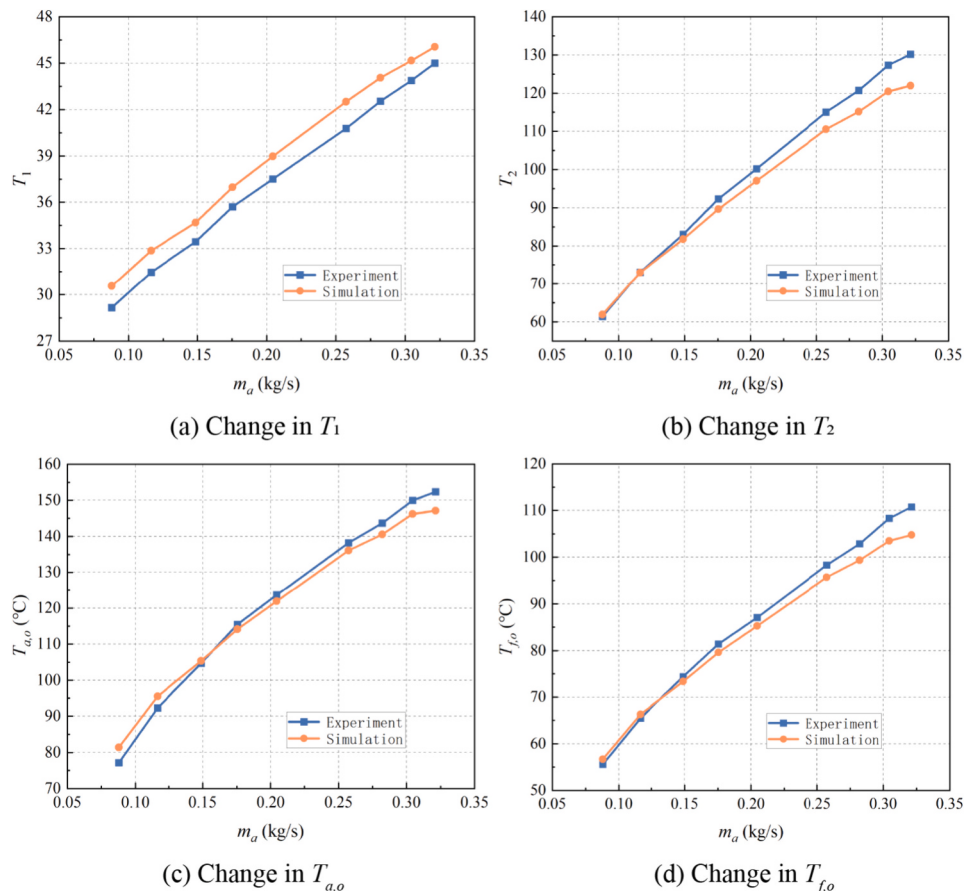


Fig. 11. Temperature variation with air mass flow rate at each node of the IHEC system.

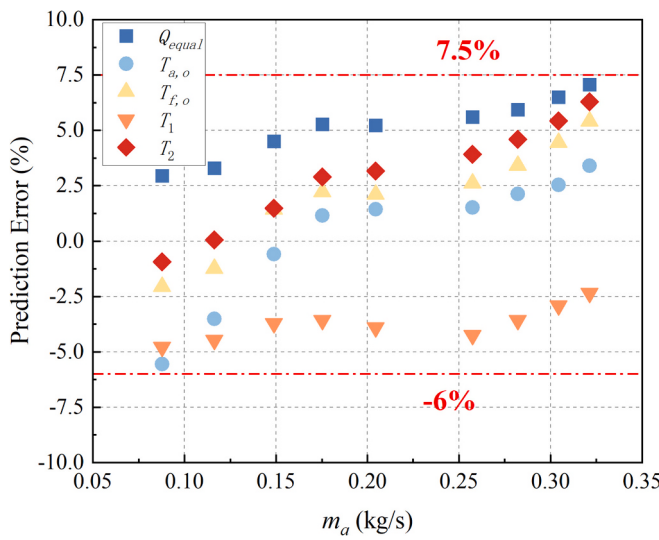
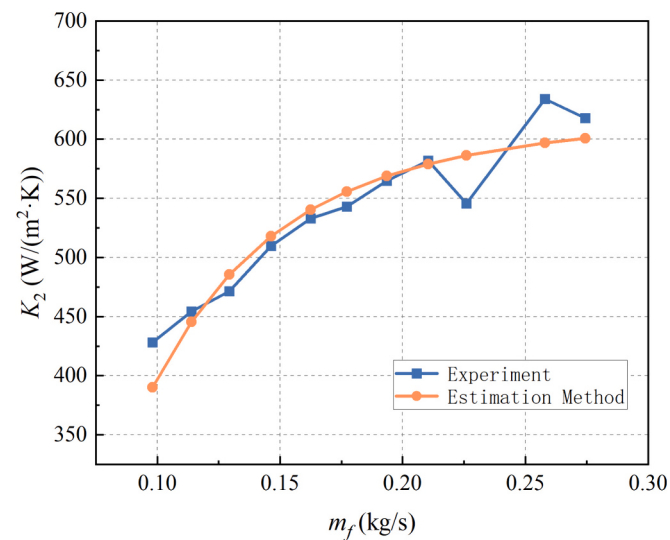


Fig. 12. Prediction errors of all parameters with different air mass flow rates.

Table 5
Experimental parameters for variable fuel mass flow rate.

Parameter	Value	Parameter	Value
m_a (kg/s)	0.202	$T_{f,i}$ (°C)	31.7–34.5
m_w (kg/s)	0.071	$P_{a,i}$ (MPa)	0.103
m_f (kg/s)	0.098–0.274	$P_{w,i}$ (MPa)	1.635
$T_{a,i}$ (°C)	248.1	$P_{f,i}$ (MPa)	3.072

Fig. 13. Comparison of K_2 as a function of m_f between experimental and estimated results.

conduction across the wall, h represents the HTC, and subscript 'c' for the cold fluid, 'h' for the hot side.

Assuming that h_h is constant and h_c varies with the flow conditions. The Dittus-Boelter formula can be employed to represent the Nusselt number (Nu) equation:

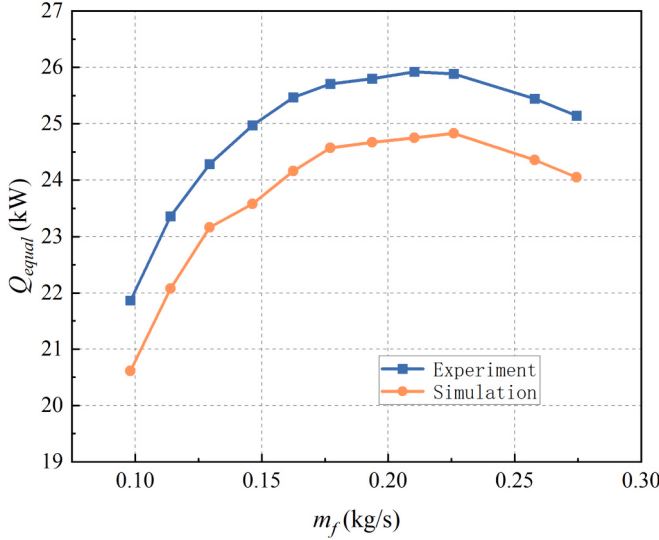


Fig. 14. Equilibrium heat transfer rate within the system variations with air mass flow rate.

$$Nu_c = C Re_c^a Pr_c^b = \frac{h_c d_c}{\lambda_c} \quad (24)$$

where C , a , and b serve as coefficients to be determined, λ_c , Pr_c , and Re_c are the thermal conductivity, Prandtl number, and Reynolds number of the cold fluid, respectively. Re_c could be expressed as:

$$Re_c = \frac{4m_c}{\mu_c \pi d_c} \quad (25)$$

where μ_c is the dynamic viscosity of the cold fluid.

Putting $\alpha = \left(\frac{4}{\mu_c \pi}\right)^a \frac{C \lambda_c Pr_c^b}{d_c^{a+1}}$ and $\beta = AR_{wall} + \frac{A}{h_h A_h}$, combining Eqs. (23)–(25) gives the expression of HTC of cold fluid and K as follows:

$$h_c = \alpha m_c^a \quad (26)$$

$$K = \frac{\frac{A_c}{A} \alpha m_c^a}{1 + \frac{A_c}{A} \alpha \beta m_c^a} \quad (27)$$

It is easy to obtain that for the case where h_c is constant and h_h varies with the flow conditions, a similar expression can be introduced. Therefore, the variation of the K of HEX with fluid mass flow rate can be expressed in the following simple form with three constants C_1 , C_2 , and C_3 .

$$K = \frac{C_1 m^{C_3}}{1 + C_2 m^{C_3}} \quad (28)$$

Based on the experimental data, the three constants can be easily determined by using the Levenberg-Marquardt algorithm. In summary, by substituting Eq. (28) into the calculation of R , the heat current method can be conveniently and efficiently applied.

3.3. Mathematical model of air inlet temperature effect

For the effects of $T_{a,i}$ on the systematic thermodynamic performance, since mass flow rates of the three working mediums are fixed, the K of HEX-1 and HEX-2 are treated as unchanging, i.e. R_1 and R_2 can be considered as constant. As a result, Eq. (16) transforms into a univariate function of Q_{equal} concerning $T_{a,i}$ and it can be reorganized as below:

$$Q_{equal} = \frac{1}{R_1 - \frac{1}{m_w c_{p,w}} + R_2} T_{a,i} - \frac{T_{f,i}}{R_1 - \frac{1}{m_w c_{p,w}} + R_2} \quad (29)$$

Substituting Eq. (29) into Eqs. (17)–(20), the following expressions are obtained, which present the impact of $T_{a,i}$ on the thermodynamic characteristics of the IHEC system. On the basis of these equations, a linear relationship with $T_{a,i}$ is evident in the behavior of these parameters.

$$T_1 = \frac{R_2 - \frac{1}{m_w c_{p,w}}}{R_1 - \frac{1}{m_w c_{p,w}} + R_2} T_{a,i} + \frac{T_{f,i} R_1}{R_1 - \frac{1}{m_w c_{p,w}} + R_2} \quad (30)$$

$$T_2 = \frac{R_2}{R_1 - \frac{1}{m_w c_{p,w}} + R_2} T_{a,i} + \frac{T_{f,i} \left(R_1 - \frac{1}{m_w c_{p,w}} \right)}{R_1 - \frac{1}{m_w c_{p,w}} + R_2} \quad (31)$$

$$T_{a,o} = \frac{m_a c_{p,a} \left(R_1 - \frac{1}{m_w c_{p,w}} + R_2 \right) - 1}{m_a c_{p,a} \left(R_1 - \frac{1}{m_w c_{p,w}} + R_2 \right)} T_{a,i} + \frac{T_{f,i}}{m_a c_{p,a} \left(R_1 - \frac{1}{m_w c_{p,w}} + R_2 \right)} \quad (32)$$

$$T_{f,o} = \frac{1}{m_f c_{p,f} \left(R_1 - \frac{1}{m_w c_{p,w}} + R_2 \right)} T_{a,i} + \frac{m_f c_{p,f} \left(R_1 - \frac{1}{m_w c_{p,w}} + R_2 \right) - 1}{m_f c_{p,f} \left(R_1 - \frac{1}{m_w c_{p,w}} + R_2 \right)} T_{f,i} \quad (33)$$

3.4. Mathematical model of air mass flow rate effect

For the effect of m_a on the systematic thermodynamic performance, considering K_1 varies with m_a , R_1 is a single-variable function relative to m_a and can be written as below:

$$R_1 = R_1(m_a) \quad (34)$$

where $R_1(m_a)$ is a function of R_1 on m_a . Substituting Eq. (34) into Eqs. (16)–(20), the thermodynamic characteristics of the effect of m_a on the system can be obtained as shown below:

$$Q_{equal} = \frac{T_{a,i} - T_{f,i}}{R_1(m_a) - \frac{1}{m_w c_{p,w}} + R_2} \quad (35)$$

$$T_1 = \frac{T_{f,i} R_1(m_a) + T_{a,i} \left(R_2 - \frac{1}{m_w c_{p,w}} \right)}{R_1(m_a) - \frac{1}{m_w c_{p,w}} + R_2} \quad (36)$$

$$T_2 = \frac{m_w c_{p,w} T_{f,i} R_1(m_a) + (m_w c_{p,w} T_{a,i} R_2 - T_{f,i})}{m_w c_{p,w} \left(R_1(m_a) - \frac{1}{m_w c_{p,w}} + R_2 \right)} \quad (37)$$

$$T_{a,o} = T_{a,i} - \frac{T_{a,i} - T_{f,i}}{m_a c_{p,a} \left(R_1(m_a) - \frac{1}{m_w c_{p,w}} + R_2 \right)} \quad (38)$$

$$T_{f,o} = T_{f,i} + \frac{T_{a,i} - T_{f,i}}{m_f c_{p,f} \left(R_1(m_a) - \frac{1}{m_w c_{p,w}} + R_2 \right)} \quad (39)$$

3.5. Mathematical model of fuel mass flow rate effect

The impact of m_f on the systematic thermodynamic performance is influenced by the variation of K_2 with m_f . As a result, the inlet temperature-based thermal resistance R_2 becomes a univariate function concerning m_f , and its expression is as follows:

$$R_2 = R_2(m_f) \quad (40)$$

where $R_2(m_f)$ is a function of R_2 on m_f . Through the substitution of Eq. (40) into Eqs. (16)–(20), the thermodynamic characteristics pertaining

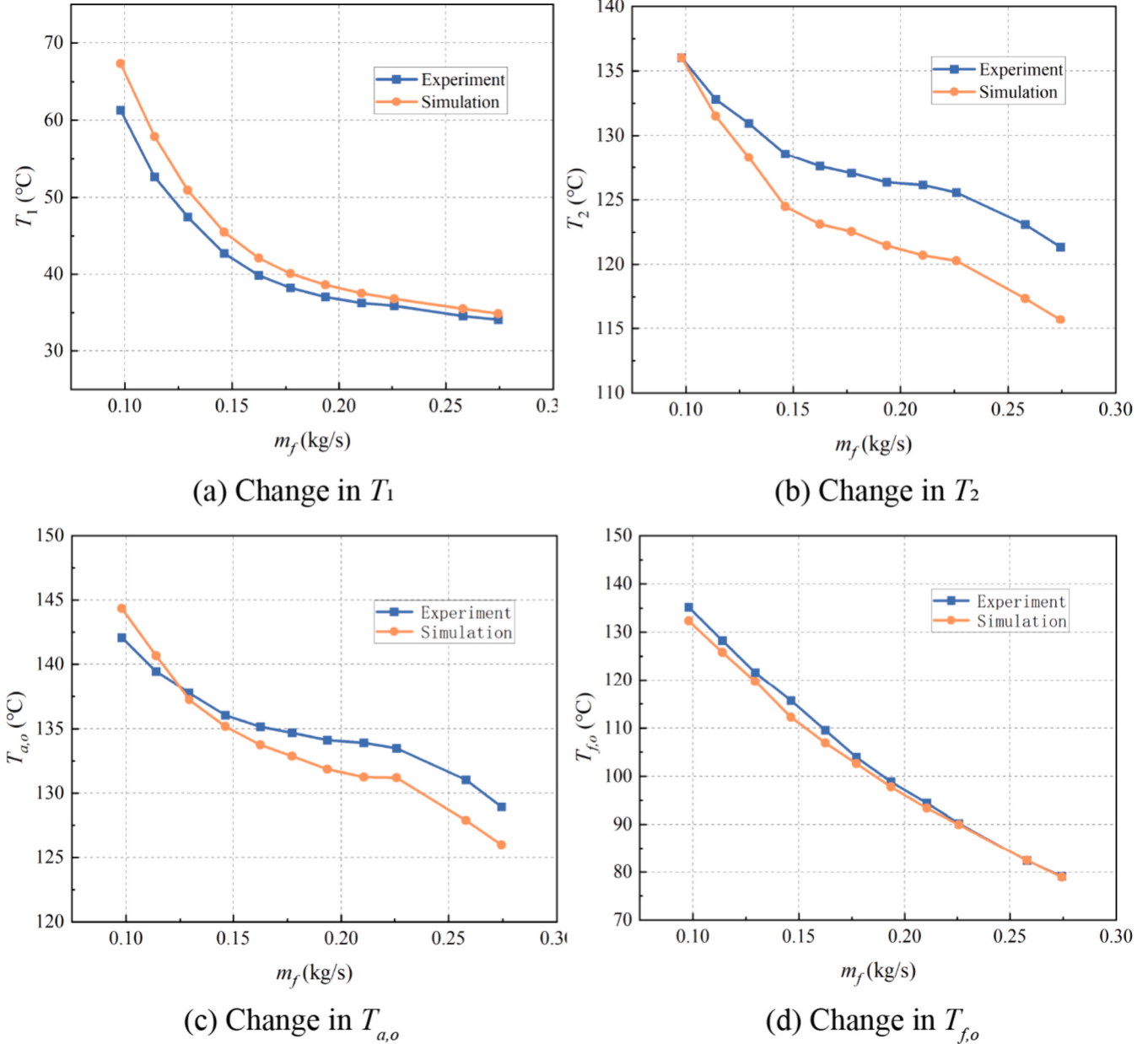


Fig. 15. Temperature variation with fuel mass flow rate at each node of the IHEC system.

to the impact of m_f on the system can be derived, as illustrated below:

$$Q_{\text{equal}} = \frac{T_{a,i} - T_{f,i}}{R_1 - \frac{1}{m_w c_{p,w}} + R_2(m_f)} \quad (41)$$

$$T_1 = \frac{T_{a,i}R_2(m_f) + \left(T_{f,i}R_1 - T_{a,i}\frac{1}{m_w c_{p,w}} \right)}{R_1 - \frac{1}{m_w c_{p,w}} + R_2(m_f)} \quad (42)$$

$$T_2 = \frac{T_{a,i}R_2(m_f) + T_{f,i}\left(R_1 - \frac{1}{m_w c_{p,w}} \right)}{R_1 - \frac{1}{m_w c_{p,w}} + R_2(m_f)} \quad (43)$$

$$T_{a,o} = T_{a,i} - \frac{T_{a,i} - T_{f,i}}{m_w c_{p,a} \left(R_1 - \frac{1}{m_w c_{p,w}} + R_2(m_f) \right)} \quad (44)$$

$$T_{f,o} = T_{f,i} + \frac{T_{a,i} - T_{f,i}}{m_f c_{p,f} \left(R_1 - \frac{1}{m_w c_{p,w}} + R_2(m_f) \right)} \quad (45)$$

3.6. Mathematical model of IWF mass flow rate effect

For effects of m_w on the systematic thermodynamic performance, taking into account that both K_1 and K_2 change with m_w , the inlet temperature-based thermal resistance R_1 and R_2 are both univariate functions of m_w , as demonstrated below:

$$\begin{cases} R_1 = R_1(m_w) \\ R_2 = R_2(m_w) \end{cases} \quad (46)$$

where $R_1(m_w)$ and $R_2(m_w)$ are the functions of R_1 and R_2 on m_w , respectively. Substituting Eq. (46) into Eqs. (16)–(20), the thermodynamic characteristics of the effect of m_w on the system can be obtained as shown below:

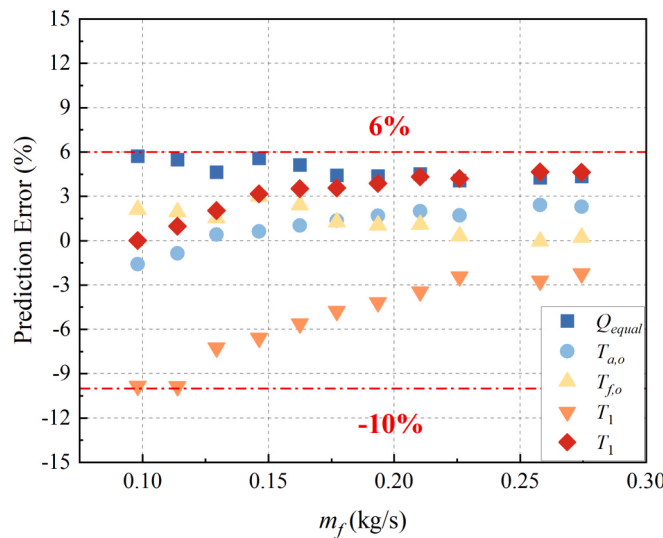


Fig. 16. Prediction errors of all parameters with different fuel mass flow rates.

Table 6
Experimental parameters for variable IWF mass flow rate.

Parameter	Value	Parameter	Value
m_a (kg/s)	0.204	$T_{f,i}$ (°C)	28.7–34.3
m_w (kg/s)	0.071–0.375	$P_{a,i}$ (MPa)	0.103
m_f (kg/s)	0.236	$P_{w1,i}$ (MPa)	1.645
$T_{a,i}$ (°C)	247.8	$P_{f,i}$ (MPa)	2.963

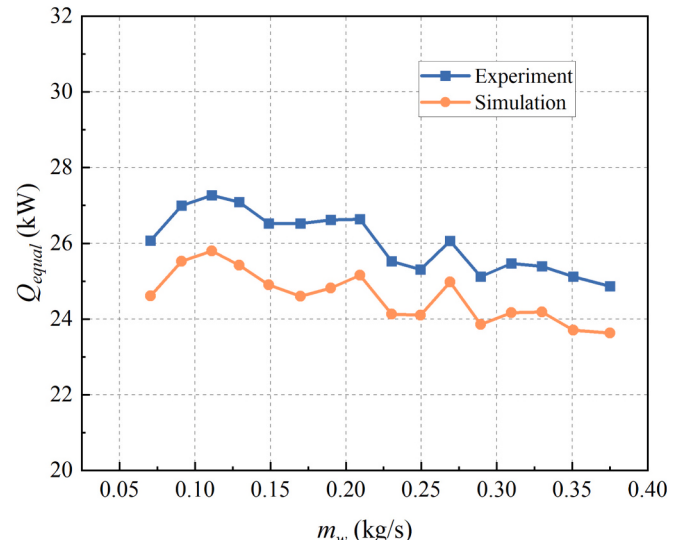
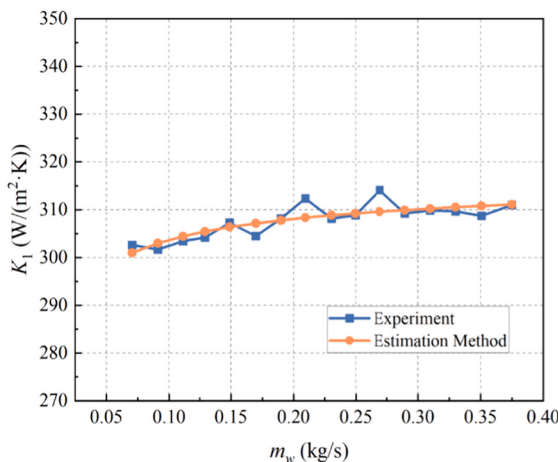
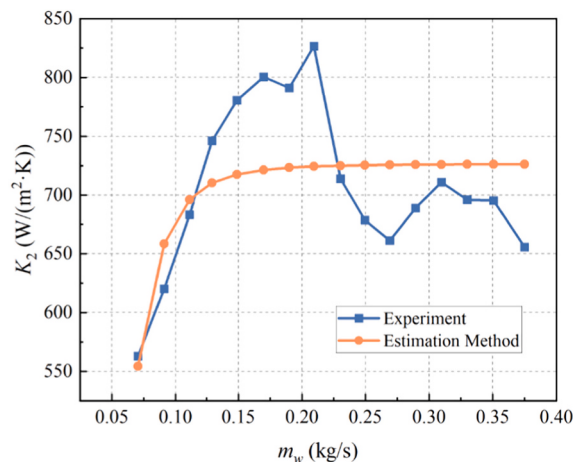


Fig. 18. Equilibrium heat transfer rate within the system variations with IWF mass flow rate.



(a) Variation of K_1



(b) Variation of K_2

Fig. 17. Comparison of overall heat transfer coefficient as a function of m_w between experimental and estimated results.

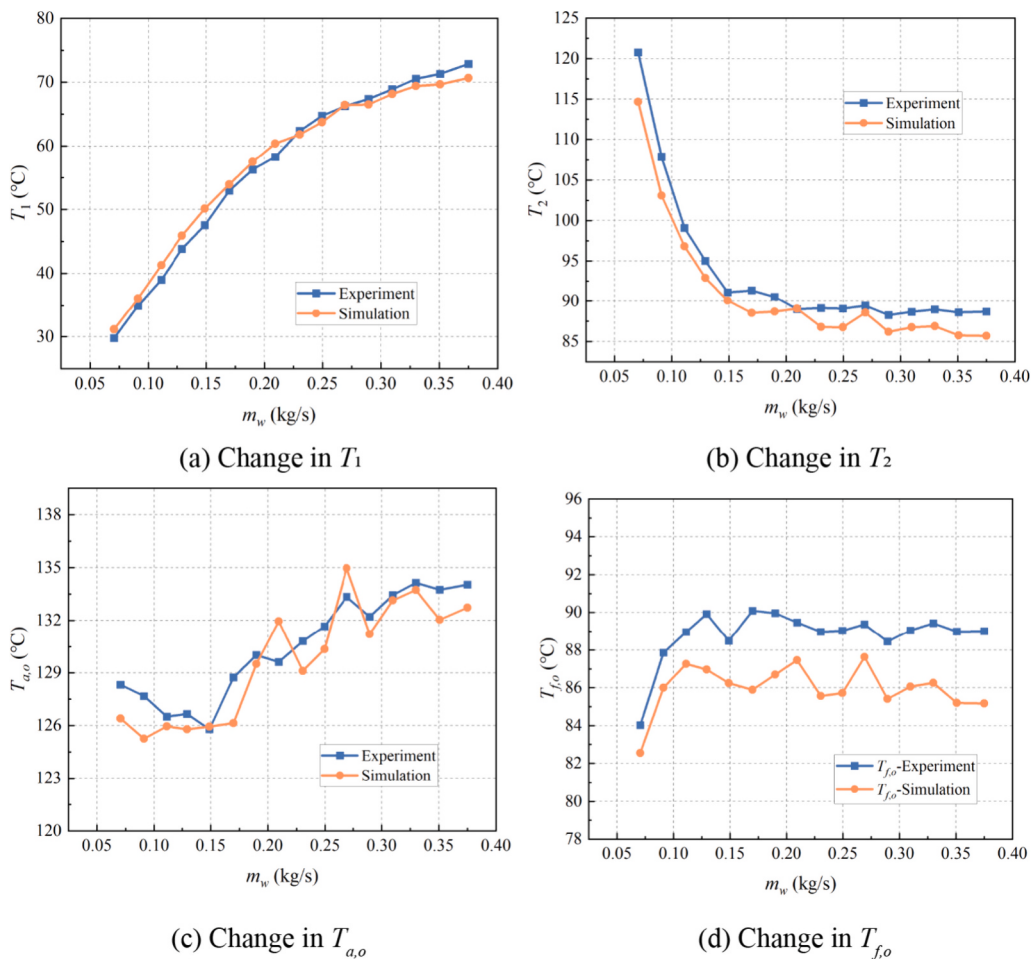


Fig. 19. Temperature variation with IWF mass flow rate at each node of the IHEC system.

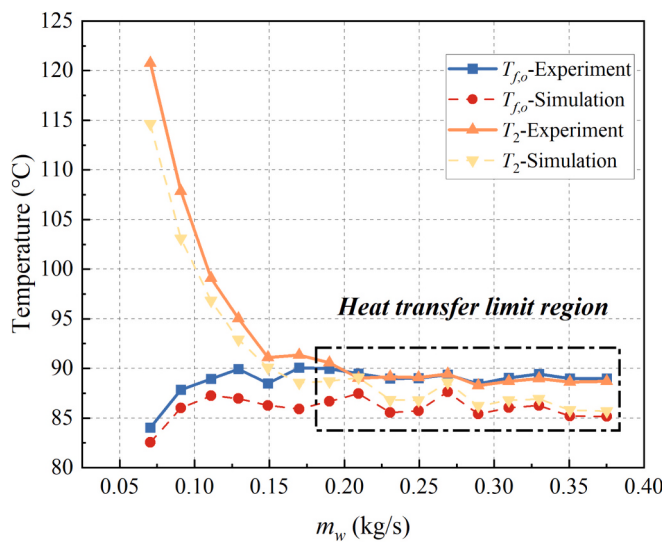


Fig. 20. Temperature variation of HEX-2 with IWF mass flow rate.

$$Q_{equal} = \frac{T_{a,i} - T_{f,i}}{R_1(m_w) - \frac{1}{m_w c_{p,w}} + R_2(m_w)} \quad (47)$$

$$T_1 = \frac{T_{a,i}R_2(m_w) + T_{f,i}R_1(m_w) - T_{a,i}\frac{1}{m_w c_{p,w}}}{R_1(m_w) - \frac{1}{m_w c_{p,w}} + R_2(m_w)} \quad (48)$$

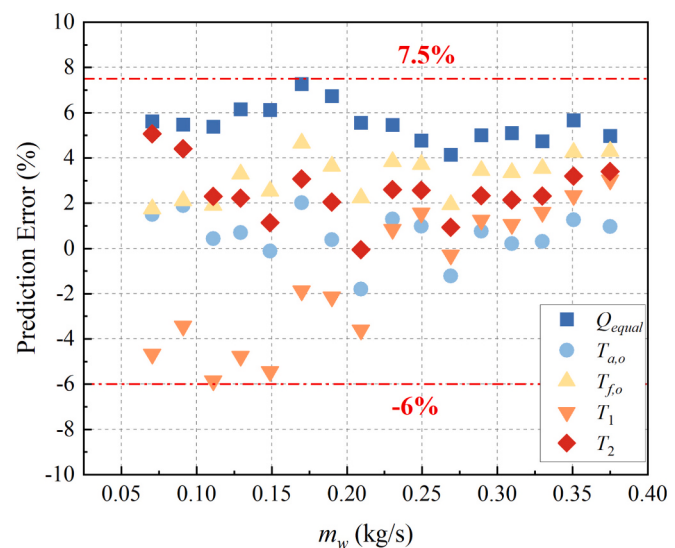


Fig. 21. Prediction errors of all parameters with different IWF mass flow rates.

$$T_2 = \frac{T_{a,i}R_2(m_w) + T_{f,i}\left(R_1(m_w) - \frac{1}{m_w c_{p,w}}\right)}{R_1(m_w) - \frac{1}{m_w c_{p,w}} + R_2(m_w)} \quad (49)$$

$$T_{a,o} = T_{a,i} - \frac{T_{a,i} - T_{f,i}}{m_a c_{p,a} \left(R_1(m_w) - \frac{1}{m_w c_{p,w}} + R_2(m_w) \right)} \quad (50)$$

$$T_{f,o} = T_{f,i} + \frac{T_{a,i} - T_{f,i}}{m_f c_{p,f} \left(R_1(m_w) - \frac{1}{m_w c_{p,w}} + R_2(m_w) \right)} \quad (51)$$

In conclusion, using the heat current method combining the K estimation method illustrates the overall thermal characteristics of the IHEC system, as shown in the above equations. These equations provide a convenient way to analyze the thermal characteristics of the system as well as to predict heat loads and temperatures.

4. Analysis of systematic thermodynamic performance

To validate the precision of the above theoretical model and investigate the influence patterns of these four parameters, the experimental investigation was conducted based on the test rig shown in [Section 2](#). The comparison of heat transfer rate between the cold and hot-side fluids for each HEX for all experimental data is plotted in [Fig. 4](#), illustrating a relative deviation within 10%, which demonstrates the reliability of the experiments.

4.1. Effect of air inlet temperature

Experiments have been conducted with varying $T_{a,i}$ and [Table 3](#) indicates the boundary conditions. Since fuel circulates through the fuel-water cooler, under circumstances of a relatively high air inlet temperature, there is a slight increase in fuel inlet temperature, limited by the cooling capacity of the fuel-water cooler. However, this does not impact the conclusion.

[Fig. 5](#) illustrates the changes in R_1 and R_2 with the increment of $T_{a,i}$. It can be observed that R_2 remains largely unchanged, while R_1 exhibits minor variations. This indicates that the assumptions made regarding thermal resistance in [Section 3.3](#) are valid. [Fig. 6](#) exhibits the changes in the Q_{equal} within the system concerning $T_{a,i}$ for both experimental and simulated results. Firstly, the experimental results closely match the simulated results obtained based on the theoretical model, confirming the accuracy of the theoretical model. Moreover, an increase in $T_{a,i}$, typically caused by a rise in flight Mach number, results in an elevated thermal load on the IHEC system, which implies a greater capacity to remove heat from the system. This phenomenon is a result of the elevated temperature difference across HEX. Based on this characteristic, for thermal management strategies of aero engines, increasing the flight Mach number, reducing the flight altitude, or increasing the pressure ratio can enable the IHEC system to transfer more heat sink, thereby raising the fuel temperature and enhancing combustion efficiency. The variation of temperature with $T_{a,i}$ at each node of the IHEC system is depicted in [Fig. 7](#). The deviation between simulated and experimental results is quite small and these parameters are approximately linearly related to $T_{a,i}$, which is consistent with the results obtained from the theoretical derivation in [Section 3.3](#). Since air is the only high-temperature heat source for the IHEC system, as $T_{a,i}$ increases, the temperature at each node of the IHEC system rises. Given that boiling of the IWF in the IHEC system should be prevented to avoid compromising system stability, therefore, in the practical application of the IHEC system, when $T_{a,i}$ increases, it is also important to monitor the T_1 and T_2 to prevent them from exceeding the boiling point.

[Fig. 8](#) presents the prediction errors of all parameters with different $T_{a,i}$. All the prediction errors between simulation and experimental values of the above five parameters of the IHEC system are less than 10%, which validates the proposed theoretical model.

4.2. Effect of air mass flow rate

[Table 4](#) indicates the boundary conditions for the tests with different m_a . Considering K_1 varies with m_a , using the proposed method for estimating the K of HEX. The comparison of K_1 as a function of m_a between experimental and estimated results is displayed in [Fig. 9](#). The maximum relative deviation between the two lines is 2.02%, which suggests the proposed method for estimating the K of HEX has high accuracy to support the application in the theoretical model.

[Fig. 10](#) depicts the changes in Q_{equal} within the system with m_a for both experimental and simulated results. At relatively low m_a (about $m_a < 0.304$ kg/s), Q_{equal} within the system increases rapidly with m_a . However, the growth of Q_{equal} gradually slows down, reaching a stable value when the m_a is high. Two key factors contribute to this phenomenon. On one hand, as m_a increases, it enhances heat transfer in HEX-1, resulting in an increase in K_1 . On the other hand, with $T_{a,i}$ held constant, the total heat from the system's high-temperature heat source increases with m_a . Nevertheless, the system's cooling source maintains a constant inlet temperature and mass flow rate, leading to a consistent maximum cooling capacity for the IHEC system. Consequently, as m_a increases, the growth of Q_{equal} gradually slows down. This indicates that the maximum heat sink transport capacity of the IHEC system is limited by the cold source, for the formulation of thermal management strategies for the IHEC system, the total amount of cold source carried by the aero engine should be fully considered. Continuously increasing the air intake will not result in an endless increase in the transported heat sink. [Fig. 11](#) presents the temperature variation with m_a at each node of the IHEC system. As observed in [Fig. 11](#) (a) and (b), the intermediate temperature increases with the increase in m_a . IWF in the intermediate circuit transfers heat through HEX-1 and K_1 increases, so the intermediate temperatures T_1 and T_2 increase, leading to the increase of fuel outlet temperature, as presented in [Fig. 11](#) (d). Since the cold-side inlet temperature of HEX-1 (T_1) increases, there is a tendency for the air outlet temperature to rise as presented in [Fig. 11](#) (c). Similar to the effect of air inlet temperature, in the practical application of the IHEC system, when adjusting the air mass flow rate, continuous attention should be given to T_1 and T_2 to avoid exceeding the IWF boiling point.

The prediction errors for various parameters across different m_a are represented in [Fig. 12](#). Notably, the prediction errors for all five parameters within the IHEC system, comparing experimental to simulated values, consistently exhibit a deviation of less than $\pm 7.5\%$, which validates the proposed theoretical model.

4.3. Effect of fuel mass flow rate

[Table 5](#) shows the boundary conditions for the tests with different m_f . Taking into account that K_2 varies with m_f , applying the proposed methodology for estimating the K of HEX. [Fig. 13](#) presents the comparison of K_2 as a function of m_f between experimental and estimated results. At relatively high fuel mass flow rates, the relative error between the two curves is a little large, reaching a maximum of approximately -7.46% . However, given the measurement uncertainty of K_2 at 5.20% shown in [Table 2](#), this relative deviation falls within an acceptable range. Consequently, the proposed K estimation method still maintains a favorable level of precision.

[Fig. 14](#) illustrates the variation of Q_{equal} within the system with m_f for both experimental and simulated results. An increase in m_f leads to enhanced heat transfer, resulting in an increase in K_2 . This enhanced fuel cooling capacity implies the ability to remove more heat from the IHEC system, hence causing an increase in Q_{equal} within the system. Similar to the situation described in [Section 4.2](#), when approaching the system's maximum cooling capacity limit, the growth of Q_{equal} gradually slows down, reaching a stable value. However, as shown in [Fig. 14](#), when m_f exceeds 0.226 kg/s, a minor downward trend in Q_{equal} is observed (with a decrease of < 1 kW). This phenomenon can be attributed to the PID feedback-controlled temperature regulation employed in the electric

heater, which induces sinusoidal oscillations in the air inlet temperature. The amplitude of these oscillations is approximately ± 7 K. For cases where m_f exceeds 0.226 kg/s, the air inlet temperature is at a trough of the sinusoidal wave, resulting in a slight decrease in Q_{equal} . As for the temperature variation with the increment of m_f at each node of the IHEC system, due to the increased cooling capacity on the cold side of HEX-2, T_1 decreases as displayed in Fig. 15 (a). Since IWF circulates in the intermediate circuit to transfer heat and the cold side inlet temperature of HEX-1 (T_1) drops, T_2 and $T_{a,o}$ decrease as illustrated in Fig. 15 (b) and (c). Besides, IWF is the cold-side working fluid of HEX-2, and its temperature decreases, leading to a decrease in fuel outlet temperature as depicted in Fig. 15 (d). For the thermal management of the IHEC system, to reduce the fuel temperature and prevent it from exceeding the maximum allowable temperature, which could lead to fuel coking and potential pipeline blockages, the fuel mass flow rate can be increased. This also brings additional benefits, such as a lower air outlet temperature, which is beneficial for subsequently cooling the turbine with the cooled air, thereby enhancing the thermal efficiency of the aero engine.

The prediction errors for various parameters across different m_f exhibit a deviation of less than $\pm 10\%$ as depicted in Fig. 16, which validates the proposed theoretical model.

4.4. Effect of IWF mass flow rate

Table 6 demonstrates the boundary conditions for the tests with different m_w . Due to the circulating flow of IWF within the intermediate circuit, variations in its mass flow rate result in changes in the K of both HEX-1 and HEX-2. Using the proposed estimation method, the comparison of the K as a function of m_w between experimental and estimated results is illustrated in Fig. 17. K_1 exhibits a better fit, with a maximum relative deviation of 1.44% observed between the two curves in Fig. 17 (a). As for K_2 , at relatively large mass flow rates (about $m_w > 0.13$ kg/s), the fitting accuracy is slightly lower, exhibiting a maximum relative deviation of 12.36% and an average relative deviation of -7.93% observed between the two curves as depicted in Fig. 17 (b). This phenomenon is attributed to the larger design margin of HEX-2. When m_w exceeds 0.13 kg/s, HEX-2 reaches its heat transfer performance limit, and the outlet temperature on the cold side approaches the inlet temperature on the hot side. This results in significant sensitivity of the LMTD calculation to experimental fluctuations, thereby leading to substantial fluctuations in the experimental results of K_2 .

The variation of Q_{equal} within the system with m_w for both simulated and experimental results is represented in Fig. 18. Unlike the situation discussed above, variations in m_w affect the K of all HEXs within the system. Additionally, thermal resistances R_1 and R_2 exhibit severe nonlinearity, as shown in Eqs. (21) and (22). As a result, Q_{equal} within the system undergoes complex oscillatory changes as a function of m_w . However, the variation of Q_{equal} within the system generally follows a downward tendency with rising m_w because of the increasing air outlet temperature ($T_{a,o}$), which is shown in Fig. 19 (c). Fig. 19 presents the variation of temperature with m_w at each node of the IHEC system. For HEX-2, IWF serves as a heat source and the total heat increases with the increase in m_w . Nevertheless, the fuel cooling capacity gradually reaches its limit, leading to simultaneous increases in heat source outlet temperature (T_1) and fuel outlet temperature of HEX-2 ($T_{f,o}$), as presented in Fig. 19 (a) and (d). As for HEX-1, IWF serves as the cooling source, as the total amount of the cold source increases, the limited air preheating capability results in a decrease in cold source outlet temperature (T_2), as demonstrated in Fig. 19 (b). For an individual HEX, an increase in the cold source mass flow rate should lead to a decrease in heat source outlet temperature. However, due to the circulating flow of IWF within the IHEC system, the increase in T_1 and the interplay between these factors result in a complex variation in the air outlet temperature, which is represented in Fig. 19 (c). Fig. 20 illustrates the variation of $T_{f,o}$ and T_2 as a function of m_w , it can be seen that when m_w exceeds 0.2 kg/s, $T_{f,o}$ and T_2 are essentially equal, indicating that HEX-2 has reached its heat

transfer performance limit, signifying an excess of heat transfer area for HEX-2 at this situation. The nonlinearity of the curves in Figs. 17–19 is primarily attributed to three factors: the high nonlinearity of the mathematical model, the complex impact of the IWF mass flow rate on the IHEC system, and the excessive heat transfer area of HEX-2 leading to its reaching the heat transfer limit.

Based on the aforementioned results, for the thermal management of the IHEC system, adjusting the IWF mass flow rate will have different effects on the system parameters. Since the IWF serves merely as a transport medium, essentially, its mass flow rate changes do not significantly affect the total amount of heat sink transferred. Increasing the m_w can reduce T_2 , which helps to prevent IWF boiling, but it will result in a higher fuel outlet temperature. Moreover, T_1 will also increase, leading to a higher working temperature of the circulating pump, thus raising the risk of its failure. Overall, the IHEC system can prevent IWF boiling by increasing the m_w , but attention must be paid to the working temperature of the circulating pump during this adjustment process to avoid exceeding its maximum allowable working temperature.

Fig. 21 displays the prediction errors of all parameters with different m_w . The prediction errors for the above five parameters within the IHEC system are less than $\pm 7.5\%$, which validates the proposed theoretical model. Besides, it reveals that the K fitting results with relatively significant fitting errors (maximum relative error of 12.36%) do not significantly affect the predictive accuracy of the heat current model for the IHEC system.

5. Conclusions

The present study constructs an experimental platform of a two-stage HEX combined IHEC system, using air, IWF, and fuel as working mediums, to experimentally investigate the thermodynamic characteristics of an IHEC system for aero engines. A theoretical analysis model of the system-level characteristics of the IHEC system has been established on the basis of the heat current method and the proposed method for estimating the K . The impact of air inlet temperature, air mass flow rate, fuel mass flow rate, and IWF mass flow rate on systematic heat transportation characteristics has been discussed. Overall, the present findings contribute to a deeper understanding of the IHEC system's behavior and offer a convenient mathematical model for its thermodynamic analysis. The following points summarize the key findings.

- (1) The proposed method for estimating the K of HEX demonstrates high accuracy. The maximum average relative deviation between the experimental and simulation values for all cases is -7.93% .
- (2) The deviation between the simulated and experimental results of system heat load and temperature at each node of the IHEC system for the four discussed situations are all less than $\pm 10\%$. This reveals the validity of the proposed thermodynamic performance analysis model built on the heat current method and K estimating model, which provides a mathematical algorithm for quickly and conveniently analyzing the thermodynamic characteristics of the IHEC system.
- (3) An increase in fuel mass flow rate leads to a decrease in temperatures at each node of the system, while the system's equilibrium heat transfer rate first increases and then stabilizes.
- (4) Variations in IWF mass flow rate can have a complex impact on the IHEC system and are influenced by the design margin and heat transfer capacity of HEXs within the system. Analysis should be tailored to the specific circumstances.

CRediT authorship contribution statement

Weitong Liu: Investigation, Data curation, Formal analysis, Software, Writing – original draft. **Guoqiang Xu:** Conceptualization, Project administration. **Xiaojia Gang:** Resources. **Han Qi:** Resources. **Mowen**

Li: Validation. **Jie Wen:** Supervision. **Yanchen Fu:** Funding acquisition, Writing – review & editing, Methodology.

Declaration of competing interest

The authors declared that they have no conflicts of interest to this work.

Data availability

Data will be made available on request.

Appendix A. Experimental data

In this appendix, the experimental data under different cases (variable air inlet temperature, air mass flow rate, fuel mass flow rate, IWF mass flow rate) are given.

	m_a (kg/s)	m_w (kg/s)	m_f (kg/s)	$T_{a,i}$ (°C)	$T_{a,o}$ (°C)	$T_{w1,i}$ (°C)	$T_{w1,o}$ (°C)	$T_{f,i}$ (°C)	$T_{f,o}$ (°C)	$T_{w2,i}$ (°C)	$T_{w2,o}$ (°C)	Q_a (kW)	Q_{w1} (kW)	Q_f (kW)	Q_{w2} (kW)
$T_{a,i}$ variation	0.204	0.102	0.235	152.04	90.08	39.69	71.46	33.97	67.00	75.32	39.50	12.82	13.61	15.41	15.35
	0.196	0.099	0.227	191.99	108.52	42.92	85.71	35.86	78.85	90.81	42.85	17.15	18.40	20.44	20.63
	0.203	0.103	0.234	274.02	146.69	49.81	116.00	40.36	104.22	123.59	48.60	26.56	28.60	31.18	32.42
	0.202	0.103	0.234	313.33	162.71	51.94	129.95	41.65	115.32	138.49	50.79	31.41	33.77	36.42	38.00
	0.203	0.103	0.234	357.20	181.81	54.77	146.04	43.25	128.62	155.71	53.82	37.04	39.58	42.82	44.23
	0.203	0.103	0.234	399.82	198.84	57.63	161.87	44.03	140.68	172.03	55.75	42.81	45.22	49.08	50.50
	0.321	0.104	0.234	248.15	152.34	44.66	126.64	35.65	110.77	133.76	45.33	31.56	35.94	36.82	38.82
	0.304	0.104	0.234	251.71	149.99	43.58	123.79	34.68	108.32	130.89	44.18	31.76	35.14	35.96	38.02
	0.282	0.104	0.235	248.13	143.64	42.24	117.34	33.82	102.87	124.04	42.84	30.20	32.87	33.52	35.56
	0.257	0.104	0.235	248.64	138.22	40.48	111.65	32.63	98.29	118.43	41.07	29.11	31.06	31.71	33.79
m_a variation	0.205	0.104	0.235	242.68	123.65	37.30	97.38	30.30	87.12	103.07	37.73	24.89	26.17	27.07	28.47
	0.175	0.104	0.235	241.90	115.45	35.57	89.44	29.17	81.40	95.28	35.83	22.65	23.42	24.72	25.86
	0.149	0.104	0.235	239.68	104.75	33.30	80.05	27.60	74.40	86.02	33.59	20.48	20.26	21.94	22.72
	0.116	0.103	0.236	241.70	92.26	31.52	71.13	26.54	65.46	75.08	31.42	17.71	17.10	18.05	18.85
	0.088	0.103	0.236	232.30	77.13	29.00	59.89	24.98	55.56	62.91	29.33	13.86	13.28	14.03	14.43
	0.202	0.071	0.274	242.41	128.93	33.81	118.21	33.69	79.10	124.46	34.46	23.44	25.15	25.13	26.84
	0.202	0.071	0.258	245.66	131.02	34.31	120.02	34.02	82.39	126.15	34.83	23.72	25.54	25.27	27.24
	0.204	0.071	0.226	250.06	133.48	35.29	122.11	34.41	90.19	128.98	36.57	24.36	25.87	25.75	27.56
	0.202	0.071	0.210	250.86	133.90	35.84	122.86	34.45	94.43	129.44	36.71	24.20	25.93	25.90	27.66
	0.203	0.071	0.194	250.53	134.13	36.48	123.22	34.41	98.82	129.47	37.66	24.21	25.86	25.72	27.40
m_f variation	0.203	0.071	0.177	251.08	134.68	37.50	123.85	34.22	103.95	130.29	39.01	24.20	25.76	25.61	27.26
	0.203	0.071	0.162	250.12	135.14	38.84	123.94	34.11	109.50	131.27	40.84	23.88	25.41	25.54	27.03
	0.203	0.071	0.146	248.72	136.04	41.32	124.74	33.96	115.71	132.40	44.07	23.41	24.94	25.10	26.44
	0.202	0.071	0.129	249.02	137.80	46.00	128.23	33.70	121.60	133.69	48.97	23.05	24.65	24.01	25.43
	0.203	0.071	0.114	246.81	139.44	50.30	129.58	33.47	128.27	136.05	55.04	22.34	23.80	22.95	24.35
	0.203	0.071	0.098	243.76	142.09	57.82	132.95	33.11	135.17	139.08	64.80	21.09	22.58	21.41	22.36
	0.204	0.070	0.236	244.19	128.33	29.06	116.62	28.73	84.03	124.92	30.52	24.22	25.86	26.32	27.90
	0.203	0.091	0.236	248.11	127.68	34.21	104.23	30.79	87.85	111.49	35.55	25.03	26.68	27.33	28.96
	0.203	0.111	0.236	249.91	126.50	37.91	95.93	31.57	88.96	102.27	40.07	25.69	26.96	27.50	28.92
	0.203	0.129	0.236	248.31	126.67	43.30	92.25	32.24	89.93	97.81	44.37	25.25	26.48	27.69	28.93
	0.204	0.149	0.236	245.30	125.79	47.03	88.87	32.59	88.50	93.36	48.05	24.94	26.07	26.82	28.25
	0.201	0.170	0.235	245.67	128.74	53.40	89.25	33.00	90.09	93.43	52.51	24.08	25.50	27.42	29.11
	0.205	0.190	0.235	248.01	130.01	56.65	88.56	33.34	89.96	92.56	55.94	24.73	25.39	27.20	29.14
m_w variation	0.204	0.209	0.235	252.62	129.62	57.52	87.00	33.30	89.47	91.04	59.05	25.66	25.86	26.95	28.08
	0.203	0.230	0.236	245.46	130.81	61.95	87.54	33.72	88.97	90.74	62.76	23.79	24.70	26.56	27.03
	0.204	0.250	0.236	246.04	131.66	64.06	87.48	33.92	89.03	90.68	65.43	23.84	24.49	26.48	26.41
	0.205	0.269	0.236	254.17	133.34	65.37	87.83	33.99	89.37	91.03	67.12	25.32	25.32	26.62	26.97
	0.204	0.289	0.235	245.52	132.21	66.99	86.79	34.07	88.46	89.75	67.77	23.66	24.03	26.11	26.68
	0.204	0.310	0.235	248.80	133.43	68.73	87.22	34.07	89.04	90.15	69.06	24.11	24.00	26.38	27.38
	0.203	0.330	0.235	250.24	134.13	70.20	87.50	34.27	89.42	90.46	70.90	24.11	23.92	26.49	27.06
	0.202	0.351	0.235	246.73	133.74	71.25	87.24	34.24	88.98	89.99	71.41	23.36	23.52	26.29	27.32
	0.204	0.375	0.235	246.16	134.03	72.50	87.39	34.33	89.00	90.03	73.22	23.37	23.42	26.24	26.44

References

- [1] A.S.J. van Heerden, D.M. Judt, S. Jafari, C.P. Lawson, T. Nikolaidis, D. Bosak, Aircraft thermal management: practices, technology, system architectures, future challenges, and opportunities, *Prog. Aerosp. Sci.* 128 (2022).
- [2] R. Welge, N+2 Supersonic Concept Development and Systems Integration: NASA/CR-2010-216842, 2010.
- [3] Z.-g. Wang, Y. Wang, J.-q. Zhang, B.-c. Zhang, Overview of the key technologies of combined cycle engine precooling systems and the advanced applications of micro-channel heat transfer, *Aerosp. Sci. Technol.* 39 (2014) 31–39.

- [4] T.T. Zhang, X.T. Yan, W. Huang, X.K. Che, Z.G. Wang, Multidisciplinary design optimization of a wide speed range vehicle with waveride airframe and RBCC engine, *Energy* 235 (2021).
- [5] S. Walker, M. Tang, C. Mamplata, TBCC propulsion for a Mach 6 hypersonic airplane, in: 16th AIAA/DLR/DGLR International Space Planes and Hypersonic Systems and Technologies Conference, 2013, p. 7238.
- [6] D. Jian, Z. Qiuru, Key technologies for thermodynamic cycle of precooled engines: a review, *Acta Astronaut.* 177 (2020) 299–312.
- [7] X. Yu, C. Wang, D. Yu, Precooler-design & engine-performance conjugated optimization for fuel direct precooled airbreathing propulsion, *Energy* 170 (2019) 546–556.
- [8] M. Togawa, T. Aoki, H. Hirakoso, T. Ito, A concept of LACE for SSTO space plane, in: 3rd International Aerospace Planes Conference, 2013, p. 5011.
- [9] L.Q. Maurice, J.L. Leingang, L.R. Carreiro, Airbreathing Space Boosters Using In-flight Oxidizer Collection 12, 1996, pp. 315–321.
- [10] B.R.A. Burns, HOTOL Space Transport for the Twenty-first Century 204, 1990, pp. 101–110.
- [11] T. Sato, N. Tanatsugu, Y. Naruo, J. Omi, Tomike Ji, T. Nishino, Development Study on ATREX Engine 47, 2000, pp. 799–808.
- [12] V. Balepin, M. Maita, S. Murthy, Third way of development of single-stage-to-orbit propulsion, *J. Propuls. Power* 16 (2000) 99–104.
- [13] R. Longstaff, A. Bond, The SKYLON project, in: 17th AIAA International Space Planes and Hypersonic Systems and Technologies Conference, 2011, p. 2244.
- [14] M. Zhang, X. Nan, D.J. Liu, Principles and Realizing Ways of Combined Power System for Pre-cooling Air Turbo Rocket 42, 2016, pp. 6–12.
- [15] P. Carter, V. Balepin, Mass injection and precompressor cooling engines analyses, in: 38th AIAA/ASME/SAE/ASEE Joint Propulsion Conference & Exhibit, 2002, p. 4127.
- [16] Z. Zou, Y. Wang, P. Du, L. Yao, S. Yang, W. Zhang, et al., A novel simplified precooled airbreathing engine cycle: thermodynamic performance and control law, *Energy Convers. Manag.* 258 (2022).
- [17] C. Wang, X. Yu, C. Ha, Z. Liu, J. Fang, J. Qin, et al., Thermodynamic analysis for a novel chemical precooling turbojet engine based on a multi-stage precooling-compression cycle, *Energy* 262 (2023).
- [18] E. Baltman, J.C. Tai, M. Shi, D.N. Mavris, An investigation of cooled cooling air for a Mach 2.2 commercial supersonic transport, in: AIAA Propulsion and Energy 2021 Forum, 2021.
- [19] W. Liu, G. Xu, Y. Fu, J. Wen, N. Zhang, Numerical investigation on forced, natural, and mixed convective heat transfer of n-decane in laminar flow at supercritical pressures, *Int. J. Heat Mass Transf.* 209 (2023).
- [20] Y. Zuo, H. Huang, Y. Fu, J. Wen, G. Xu, Vibration effects on heat transfer characteristics of supercritical pressure hydrocarbon fuel in transition and turbulent states, *Appl. Therm. Eng.* 219 (2023).
- [21] A. Duncan Walker, B. Koli, L. Guo, P. Beecroft, M. Zedda, Impact of a cooled cooling air system on the external aerodynamics of a gas turbine combustion system, *J. Eng. Gas Turbines Power* 139 (2017).
- [22] L. Zhuang, G. Xu, Q. Liu, M. Li, B. Dong, J. Wen, Superiority analysis of the cooled cooling air technology for low bypass ratio aero-engine under typical flight mission, *Energy Convers. Manag.* 259 (2022).
- [23] S. Pandey, H. Kallath, H.Y. Choi, T. Sibili, J.K. Min, J. Chetwynd-Chatwin, et al., Numerical study of the effect of flow nonuniformities on the low-pressure side of a cooled cooling air heat exchanger, *Appl. Therm. Eng.* 217 (2022).
- [24] Y. Fu, W. Liu, H. Qi, Q. Chen, J. Wen, G. Xu, Heat transfer area optimization of intermediate heat-exchange cycle system for aero engines, *Int. J. Heat Mass Transf.* 220 (2024).
- [25] K. Kasim, A. Muley, M. Stoia, F. Ladeinde, Advanced heat transfer devices for aerospace applications, in: ASME 2017 International Mechanical Engineering Congress and Exposition, 2017.
- [26] H. Chang, J. Lian, T. Ma, L. Li, Q. Wang, Design and optimization of an annular air-hydrogen precooler for advanced space launchers engines, *Energy Convers. Manag.* 241 (2021).
- [27] W. Affonso, R. Gandolfi, R.J.N. dos Reis, C.R.I. da Silva, N. Rodio, T. Kipouros, et al., Thermal management challenges for HEA – FUTPRINT 50, in: IOP Conference Series: Materials Science and Engineering, 2021, p. 1024.
- [28] J.-l. Liu, S. Wang, T.-Y. Zhang, Y.-l. Wang, K.-l. He, Z. Cui, et al., Experiment and simulation on a thermal management scheme of intermediate circulation based on heat current method, *Int. J. Heat Mass Transf.* (2023) 206.
- [29] D. Sighorsson, M.W. Oppenheimer, D.B. Doman, Aircraft thermal endurance enhancement using a dual tank configuration and temperature regulation, in: 2018 AIAA Guidance, Navigation, and Control Conference, 2018.
- [30] M.W. Oppenheimer, D. Sighorsson, D.B. Doman, Control of fuel thermal management systems with transport delays, in: AIAA Scitech 2019 Forum, 2019.
- [31] Y. Liu, G. Xu, Y. Fu, J. Wen, H. Huang, Thermal dynamic and failure research on an air-fuel heat exchanger for aero-engine cooling, *Case Stud. Therm. Eng.* (2023) 42.
- [32] N.R. Herring, S.D. Heister, Review of the development of compact, high performance heat exchangers for gas turbine applications, in: ASME International Mechanical Engineering Congress and Exposition, 2006, pp. 467–476.
- [33] M. Colera, Á. Soria, J. Ballester, A numerical scheme for the thermodynamic analysis of gas turbines, *Appl. Therm. Eng.* 147 (2019) 521–536.
- [34] R.S. Kamath, L.T. Biegler, I.E. Grossmann, An equation-oriented approach for handling thermodynamics based on cubic equation of state in process optimization, *Comput. Chem. Eng.* 34 (2010) 2085–2096.
- [35] M. Arnold, Stability of sequential modular time integration methods for coupled multibody system models, *J. Comput. Nonlinear Dyn.* 5 (2010).
- [36] T. Zhao, X. Chen, K.-L. He, Q. Chen, A standardized modeling strategy for heat current method-based analysis and simulation of thermal systems, *Energy* 217 (2021).
- [37] Z.-Y. Guo, H.-Y. Zhu, X.-G. Liang, Entransy—A physical quantity describing heat transfer ability, *Int. J. Heat Mass Transf.* 50 (2007) 2545–2556.
- [38] Q. Chen, J.-H. Hao, T. Zhao, An alternative energy flow model for analysis and optimization of heat transfer systems, *Int. J. Heat Mass Transf.* 108 (2017) 712–720.
- [39] Q. Chen, Entransy dissipation-based thermal resistance method for heat exchanger performance design and optimization, *Int. J. Heat Mass Transf.* 60 (2013) 156–162.
- [40] X. Li, Q. Chen, J.H. Hao, X. Chen, K.L. He, Heat current method for analysis and optimization of a refrigeration system for aircraft environmental control system, *Int. J. Refrig.* 106 (2019) 163–180.
- [41] G. Shen, F. Yuan, Y. Li, W. Liu, The energy flow method for modeling and optimization of organic Rankine cycle (ORC) systems, *Energy Convers. Manag.* 199 (2019).
- [42] K.-L. He, T. Zhao, H. Ma, Q. Chen, Optimal operation of integrated power and thermal systems for flexibility improvement based on evaluation and utilization of heat storage in district heating systems, *Energy* 274 (2023).
- [43] T. Zhao, Y. Min, Q. Chen, J.-H. Hao, Electrical circuit analogy for analysis and optimization of absorption energy storage systems, *Energy* 104 (2016) 171–183.
- [44] K. Goudarzi, A. Moosaei, M. Gharaati, Applying artificial neural networks (ANN) to the estimation of thermal contact conductance in the exhaust valve of internal combustion engine, *Appl. Therm. Eng.* 87 (2015) 688–697.
- [45] A. Rahman, X. Zhang, Prediction of oscillatory heat transfer coefficient for a thermoacoustic heat exchanger through artificial neural network technique, *Int. J. Heat Mass Transf.* 124 (2018) 1088–1096.
- [46] Y. Qiu, D. Garg, L. Zhou, C.R. Kharangate, S.-M. Kim, I. Mudawar, An artificial neural network model to predict mini/micro-channels saturated flow boiling heat transfer coefficient based on universal consolidated data, *Int. J. Heat Mass Transf.* 149 (2020).
- [47] A. Faraj, J. Faraj, E. Harika, F. Hachem, M. Khaled, Development of a new method for estimating the overall heat transfer coefficient of heat exchangers – validation in automotive applications, *Case Stud. Therm. Eng.* (2021) 28.
- [48] E. Lemmon, M.L. Huber, M.O. McLinden, NIST standard reference database 23: reference fluid thermodynamic and transport properties-REFPROP, version 8.0, 2007.
- [49] H. Deng, C. Zhang, G. Xu, Z. Tao, B. Zhang, G. Liu, Density measurements of endothermic hydrocarbon fuel at sub-and supercritical conditions, *J. Chem. Eng. Data* 56 (2011) 2980–2986.
- [50] H. Deng, K. Zhu, G. Xu, Z. Tao, C. Zhang, G. Liu, Isobaric specific heat capacity measurement for kerosene RP-3 in the near-critical and supercritical regions, *J. Chem. Eng. Data* 57 (2012) 263–268.
- [51] J. Taylor, Introduction to error analysis, the study of uncertainties in physical measurements, 1997.
- [52] Y. Fu, Y. Liu, J. Wang, Y. Wang, G. Xu, J. Wen, Local resistance characteristics of elbows for supercritical pressure RP-3 flowing in serpentine micro-tubes, *Props., Power. Res.* (2024).
- [53] Y. Fu, B. Bian, Y. Liu, L. Zhang, M. Li, J. Wen, G. Xu, Airside heat transfer analysis using Wilson plot method of three analogous serpentine tube heat exchangers for aero-engine cooling, *Appl. Therm. Eng.* 248 (2024).